

High resolution cryo-EM and crystallographic snapshots of the actinobacterial two-in-one 2-oxoglutarate dehydrogenase

Received: 23 February 2023

Accepted: 19 July 2023

Published online: 10 August 2023

 Check for updatesLu Yang^{1,2}, Tristan Wagner^{1,4}, Ariel Mechaly³, Alexandra Boyko^{1,5}, Eduardo M. Bruch^{1,6}, Daniela Megrian¹, Francesca Gubellini¹, Pedro M. Alzari¹ & Marco Bellinzoni¹✉

Actinobacteria possess unique ways to regulate the oxoglutarate metabolic node. Contrary to most organisms in which three enzymes compose the 2-oxoglutarate dehydrogenase complex (ODH), actinobacteria rely on a two-in-one protein (OdhA) in which both the oxidative decarboxylation and succinyl transferase steps are carried out by the same polypeptide. Here we describe high-resolution cryo-EM and crystallographic snapshots of representative enzymes from *Mycobacterium smegmatis* and *Corynebacterium glutamicum*, showing that OdhA is an 800-kDa homohexamer that assembles into a three-blade propeller shape. The obligate trimeric and dimeric states of the acyltransferase and dehydrogenase domains, respectively, are critical for maintaining the overall assembly, where both domains interact via subtle readjustments of their interfaces. Complexes obtained with substrate analogues, reaction products and allosteric regulators illustrate how these domains operate. Furthermore, we provide additional insights into the phosphorylation-dependent regulation of this enzymatic machinery by the signalling protein OdhI.

Acyl-CoA esters are the major metabolic carriers of carbon units in living organisms. The most conserved ways to their synthesis include the oxidative decarboxylation of 2-oxoacids carried out by three main dehydrogenase complexes: the pyruvate dehydrogenase complex (PDHc), that feeds acetyl-CoA units into the TCA cycle, the branched-chain ketoacid dehydrogenase complex (BCKDH) involved in the catabolism of leucine, isoleucine and valine, and the 2-oxoglutarate dehydrogenase complex (ODH; also known as α -ketoacid dehydrogenase, or KDH), which catalyses the synthesis of succinyl-CoA within the TCA cycle¹. Other substrate specificities have also been reported, one of the most known examples being the 2-oxoadipate dehydrogenase complex which, in human, shares

subunits with ODH and is devoted to the degradation of 2-oxoadipate from the L-lysine degradation pathway^{2–4}. These enzymatic machineries are made by multiple copies of three enzyme components: the E1 component catalyses the thiamine diphosphate (ThDP)-dependent decarboxylation of the 2-oxoacid and its transfer to a lipoyl-lysine group, E2 transfers this acyl-moiety to the CoASH acceptor to generate acyl-CoA, and E3 is a FAD-dependent dehydrogenase that uses NAD⁺ to oxidize the dihydrolipoyl moiety, generating NADH⁵. One or more lipoyl domains, which shuttle between the E1, E2 and E3 active sites, are covalently connected to the E2 catalytic domain through flexible linkers acting as swinging arms¹.

¹Institut Pasteur, Université Paris Cité, CNRS UMR3528, Unité de Microbiologie Structurale, F-75015 Paris, France. ²Wuhan Institute of Biological Products Co. Ltd., Wuhan 430207, PR China. ³Institut Pasteur, Université Paris Cité, Plateforme de Cristallographie, F-75015 Paris, France. ⁴Present address: Microbial Metabolism Group, Max Planck Institute for Marine Microbiology, Celsiusstraße 1, D-28359 Bremen, Germany. ⁵Present address: BostonGene, Yerevan, Armenia. ⁶Present address: Sanofi, In vitro Biology, Integrated Drug Discovery, 350 Water St, Cambridge, MA 02141, USA.

✉ e-mail: marco.bellinzoni@pasteur.fr

These ubiquitous complexes among aerobic organisms have long been thought to share a universally conserved architecture, characterized by a large hollow central core composed of multiple copies of the E2 catalytic domain, with a symmetry depending on the complex and the species^{1,6}. The highly symmetric nature of the E2 core was first described by pioneer electron microscopy and X-ray crystallography studies^{7,8}, and largely confirmed afterwards^{9–12}. The two other complex components, i.e. E1 and E3, are tethered to the core through the peripheral subunit binding domain (PSBD) located on the protruding E2 swinging arms^{13,14}. Although such interactions have been characterized and the structure of separate subcomplexes reported^{15–20},

the intrinsic flexible nature of the E2 swinging arms has long hampered attempts to perform high-resolution structural studies of these complexes in their entirety. Progress has been made recently, with single particle cryo-EM studies that have shed light on dihydrolipoyl-lysine channeling within the E2 core of *E. coli* PDHc²¹, among the most studied models for such complexes, as well as on the role of the E3 binding protein (E3BP) that is also part of the inner core in eukaryotic PDH complexes^{22–24}.

These highly conserved principles of 2-oxoacid dehydrogenase assembly, however, are not followed in Actinobacteria, one of the largest bacteria phyla. Earlier work had shown that *Corynebacterium glutamicum*, a well-known actinobacterial model largely used for biotechnological applications, possesses an enzyme, called OdhA, which bears succinyltransferase (E2o) and 2-oxoglutarate decarboxylase (E1o) domains on the same polypeptide^{25–27}, a feature shared by the mycobacterial homolog KGD²⁸. Considering the presence of such a ‘two-in-one’ fusion enzyme, which depends on lipoyl-lysine provided in trans as an acyl group carrier, and that E2p was reported to be the only lipoylated protein in *M. tuberculosis*²⁹ and in *C. glutamicum*²⁶, it was proposed that PDH and ODH may form a mixed supercomplex in those species, a hypothesis corroborated by the copurification of OdhA with components of the PDH complex in *C. glutamicum*²⁷. The three-dimensional architecture of OdhA has however remained unknown so far, raising questions not only on how domains characterized by different oligomeric states may be arranged in the same polypeptide, but also about the composition, the size and the assembly of such a mixed PDH/ODH supercomplex. In addition, challenging even further the current ‘dogma’ of the universal conservation of PDH and ODH complexes, we recently showed that AceF (E2p) in actinobacterial PDH is reduced to its minimally active trimeric unit, due to a three-residue insertion at its C-terminal end that hinders any trimer-trimer interaction³⁰. We also proposed that the presence of the C-terminal insertion and that of an *odhA*-like gene are related and constitute a signature of the Actinobacteria class³⁰.

Here, we show by X-ray crystallography and high-resolution cryo-EM, that corynebacterial OdhA and its mycobacterial orthologue KGD are large (~0.8 MDa) homo-hexameric enzymes with an unprecedented molecular architecture, and discuss how intra and interdomain interactions may account for their unusual regulatory properties.

Results

Actinobacterial OdhA/KGD is an 800 kDa homo-hexamer with two distinct catalytic centers

Our previous work with an N-terminal truncated form of *Mycobacterium smegmatis* KGD (*MsKGD*_{Δ115} construct designed based on limited trypsin proteolysis of the full-length protein) revealed the structure of the active E1o homodimer, in which each protomer was tightly associated to a monomeric E2o-like domain²⁸. Since the acyltransferase catalytic activity is located at the junction of two E2 protomers³¹, the obtained structure cannot reflect an active E2o state, and we hypothesized that the N-terminal truncation may have interfered with the assembly of the obligate homotrimeric state of this domain. We therefore decided to produce in *E. coli* the full-length proteins KGD from *M. smegmatis* and OdhA from *C. glutamicum* for further studies. Crystals were obtained for both proteins, but their X-ray diffraction was too limited for structural characterization. Therefore, we first proceeded by co-crystallizing *MsKGD* with the inhibitor GarA for further stabilization, and we solved the structure of the *MsKGD*-GarA complex at 4.6 Å resolution using the previously published *MsKGD*_{Δ115} structure²⁸ as the search model (Table 1). *MsKGD* presents an homo-hexameric assembly (Fig. 1), which can be described as a three-blade, triangular propeller shape, approximately 20 nm wide and 15 nm thick. The E1o dimers containing the Mg-ThDP compose the blades, with two central E2o trimers sitting respectively on either side of the blades plane. This oligomeric arrangement as a trimer of dimers allows the

Table 1 | Crystallographic data collection and refinement statistics

Dataset	<i>MsKGD</i> -GarA	<i>OdhA</i> _{Δ97}
Synchrotron beamline	SOLEIL Proxima 1	ESRF ID30A-3
Wavelength (Å)	0.9763	0.9677
Space group	P 6 ₅	H 3 2
Unit cell parameters		
a, b, c (Å)	325.75, 325.75, 396.94	150.99, 150.99, 314.34
α, β, γ (°)	90.00, 90.00, 120.00	90.00, 90.00, 120.00
Resolution (Å) ^a	282.11 – 4.56 (4.78 – 4.56)	100.52 – 2.46 (2.70 – 2.46)
R _{pim} ^b	0.076 (0.583)	0.047 (0.466)
I/σ(I)	8.1 (1.5)	15.5 (1.6)
Completeness (%)	94.6 (52.9)	94.4 (63.8)
CC(1/2)	0.998 (0.701)	0.998 (0.658)
Multiplicity	11.5 (11.8)	10.4 (8.5)
Refinement		
Resolution (Å)	4.56	2.46
No. reflections	121081	38238
R _{work} /R _{free} (%) ^c	19.8 / 22.9	20.4 / 25.1
No. atoms		
Protein	56835	8366
Ligands/ions	170	109
Solvent	–	397
Average B-factors		
Protein	236.15	59.22
Ligand/ions	222.98	76.32
Solvent	–	49.85
R.m.s deviations ^d		
Bond lengths (Å)	0.009	0.011
Bond angles (°)	1.278	1.458
Validation ^d		
MolProbity score	2.40	1.20
Clashscore	8.15	1.56
Poor rotamers (%)	4.56	1.71
Ramachandran plot ^d		
Favored (%)	92.72	97.41
Allowed (%)	6.94	2.59
Outliers (%)	0.34	0.00
PDB accession code	8P5R	8P5S

^aResolution limits were determined by applying an anisotropic high-resolution cut-off via STARANISO, part of the autoPROC data processing software³²; values in parentheses refer to the highest resolution shell.

^bR_{pim} = $\sum_{hkl} [1/(N-1)]^{1/2} \sum_i |I_i(hkl) - \langle I \rangle(hkl)| / \sum_i I_i(hkl)$, where N is the multiplicity, I_i is the intensity of reflection i and $\langle I \rangle(hkl)$ is the mean intensity of all symmetry-related reflections.

^cR_{work} = $\sum |F_o| - |F_c| / \sum |F_o|$, where F_o and F_c are the observed and calculated structure factor amplitudes. Five percent of the reflections were reserved for the calculation of R_{free}.

^dValues from MOLPROBITY³³.

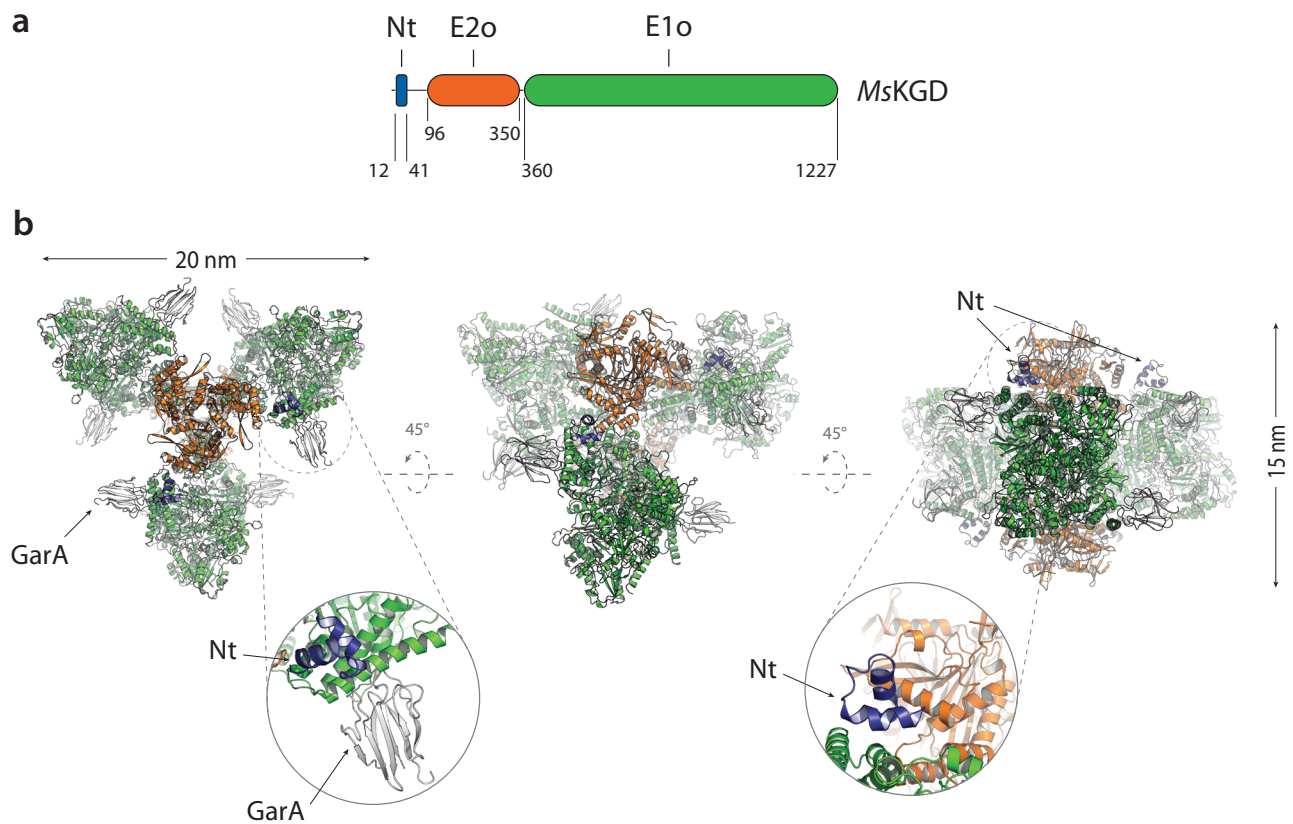


Fig. 1 | *MsKGD* domain boundaries and crystal structure of the *MsKGD*-*GarA* complex. **a** Domain boundaries in *MsKGD* (Nt: N-terminal helical domain) and **(b)** cartoon overview of the *MsKGD* hexamer in complex with *GarA* (gray). Zoomed

views highlighting the position of the N-terminal helical hairpin (blue) are shown below. Crystal structure determined at 4.6 Å resolution.

separate E1o and E2o domains to maintain their canonical oligomeric arrangements (i.e. E1o dimers and E2o trimers) as seen in other oxoacid dehydrogenases, with their functional catalytic centers at the respective oligomeric interfaces. The inhibitor *GarA* binds full-length *MsKGD* in the same way as previously described for the high-resolution structure of the *GarA*-*MsKGD*_{Δ360} complex³² (Supplementary Fig. 1), and the *MsKGD* E1o domain is indeed held in the resting conformation, as a result of *GarA* binding³². Interestingly, the low-resolution crystal structure also shows clear electron density, in four out of the six protomers, for a short helical hairpin engaged in intermolecular interactions (Fig. 1b), which could be attributed to the N-terminal helical segment^{26,28}. These observations suggest that the N-terminal domain of *MsKGD* and *OdhA* could be involved in protein-protein interactions with other components of the complex, as it was recently reported for human³³ and bovine *ODH*³⁴.

In parallel, the characterization of recombinant *C. glutamicum* *OdhA* showed a specific 2-oxoglutarate decarboxylase activity of 110.3 ± 1.0 nmol/min/mg, consistent with previous reports (Supplementary Table 1)²⁶, and an *ODH* activity of 68.6 ± 0.6 nmol/min/mg when integrated in a reconstituted *PDH/ODH* supercomplex with recombinant *AceE* (E1p), *AceF* (E2p) and *Lpd* (E3) from the same species in equimolar ratios, a value higher than reported elsewhere under similar conditions³⁵ but compatible with measurements made on *C. glutamicum* cell extracts (Supplementary Table 1). The same reconstituted supercomplex showed a lower *PDH* specific activity (3.3 ± 0.3 nmol/min/mg), which however raised to 14.5 ± 0.4 nmol/min/mg when *OdhA* was omitted (Supplementary Table 1), suggesting that *OdhA* and *AceE* may compete for the available lipoyl groups, consistently with *AceF* being required for both the *PDH* and *ODH* reactions²⁶. On the other hand, purified *OdhA* showed a sedimentation

coefficient of 16.8 S (Supplementary Fig. 2) suggesting a predominant homohexameric state in solution, at all the tested concentrations. Therefore, based on the *MsKGD* structure and on secondary structure predictions, we produced a truncated version of *OdhA* deprived of the flexible N-terminal segment (*OdhA*_{Δ97}), which produced crystals diffracting up to 2.5 Å resolution (Table 1). As *OdhA* indeed presents the same homohexameric assembly as *MsKGD* (Fig. 2), all further structural analyses in this work will be focused on the higher resolution *OdhA* model. The single protomer shows the presence of an N-terminal acyltransferase (E2o) domain, spanning from the construct N-terminus to residue Asn349, connected by a 17-residue linker to the C-terminal, ThDP-dependent oxoglutarate dehydrogenase domain (E1o) (Supplementary Fig. 3). In turn, the latter is made by a small helical domain (residues Asp367-Thr448) followed by three consecutive α/β subdomains, characteristic of homodimeric transketolases (Supplementary Fig. 3). In addition, a ThDP-Mg²⁺ cofactor is bound at the E1o domain dimeric interface (Fig. 2a), in an equivalent pose and active site environment as in the *M. smegmatis* E1o (*MsKGD*_{Δ360}) high-resolution crystal structures^{28,36}. On the other hand, the E2o N-terminal domain shows the known, compact triangular trimeric conformation of the chloramphenicol acetyltransferase (CAT) family, characterized by an N-terminal β-strand that protrudes to make a strand exchange (mixed β-sheet) with the neighboring monomer (Supplementary Fig. 4). The absence of such β-strand and the following α-helix in the *MsKGD*_{Δ115} construct may therefore explain initial failures in observing a functional E2o assembly²⁸. Furthermore, despite the overall conservation of the CAT fold, a notable difference between the *OdhA* succinyltransferase domain and other E2o domains resides in the β-hairpin that normally lies close to the three-fold axis and is located on the inside surface of the cubic assembly, here replaced by a short α-helix

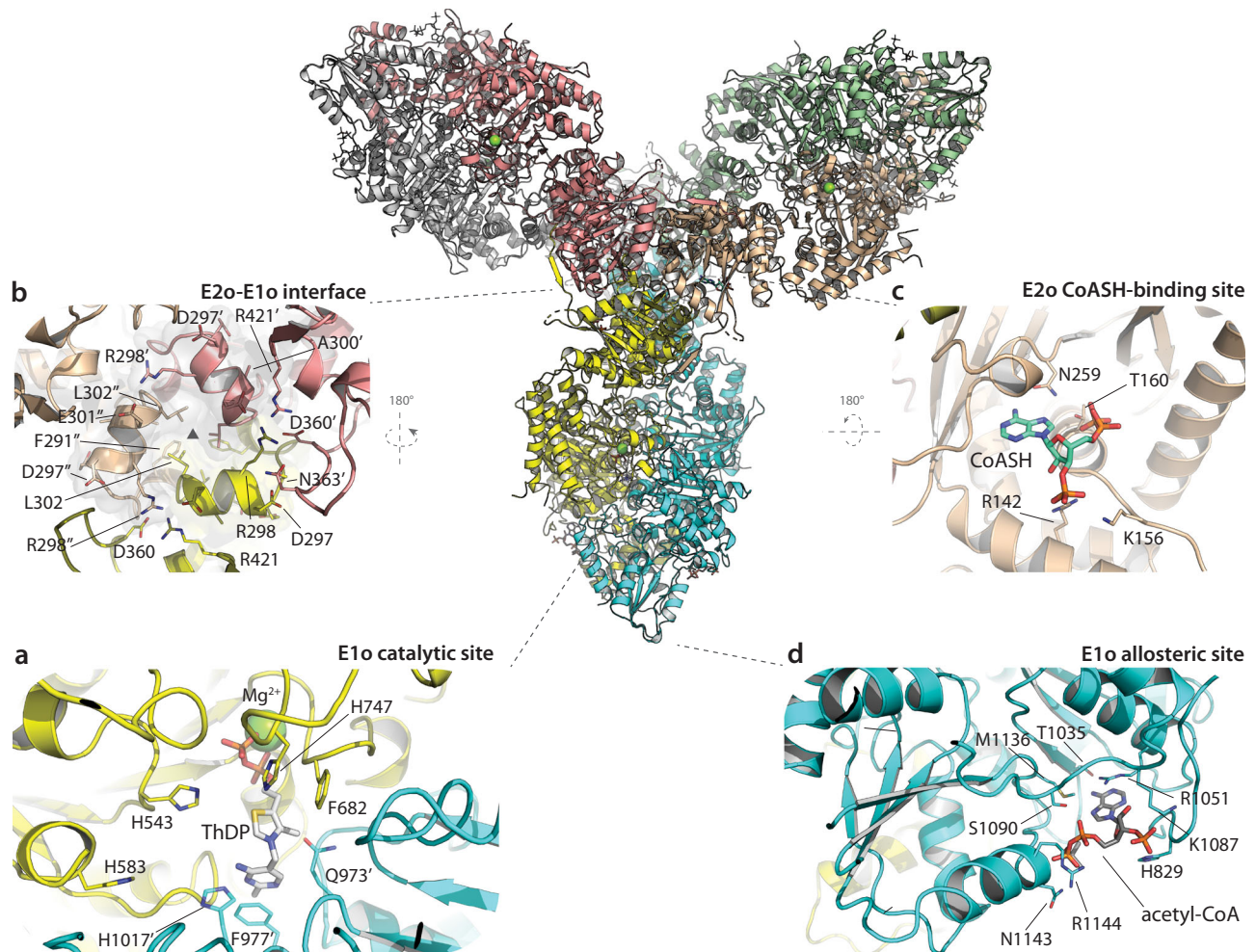


Fig. 2 | Crystal structure of *OdhA*_{Δ97} with focus on the E2o/E1o interface and on catalytic and allosteric sites. Center: cartoon overview of the *OdhA*_{Δ97} homo-hexamers (one color per chain), with the single protomers related by crystallographic symmetry. Laterally, clockwise: **a** E1o catalytic site at the protomer interface, the ThDP-Mg²⁺ cofactor at the center; **b** view, from the inside face, of the E2o-E1o interface along the E2o domain 3-fold axis (triangle), highlighting the symmetric intra- and intersubunit interactions of the short α -helix Glu296-Leu302

(see also Supplementary Fig. 4); **c** E2o CoASH binding site (CoASH pantothenate chain not traced due to lack of supporting electron density); **d** E1o allosteric acetyl-CoA binding site (pantothenate chain also not traceable). Indicated in the figure and depicted as sticks are residue side chains interacting with cofactor or ligands (**a**, **c**, **d**), involved in contacts at the domain interface (**b**) or with a predicted role in catalysis (namely His543, His583, His747 and His1017, as reported for *MskGD*²⁸).

(connected by flexible linkers) spanning residues 296-302 (Fig. 2b; Supplementary Fig. 4). This helix interacts both with its symmetric counterparts from the neighboring domains around the E2o three-fold axis, notably through a strong salt bridge involving Glu301 and Arg298, but also makes contacts with the E1o domains (Fig. 2b), both intrasubunit (the Ala300 carbonyl oxygen is well positioned to hydrogen bond to Arg421) and intersubunit, another H-bond involving the carboxyl group of Asp297 and the main chain amide of Asn363 from the nearby chain (Fig. 2b). The three-fold symmetric packing of the 296-302 α -helix is further stabilized by hydrophobic interactions between the side chains of Phe291 and Leu302, positioned internally (Fig. 2b). The structural alignment of the *OdhA* and *MskGD* E2o domains with characterized acyltransferase domains from other E2 enzymes confirms that this α -helix arises from a sequence insertion (Supplementary Fig. 5), and suggest it to be a structural feature of *OdhA*-like enzymes, likely as an adaptation to E2o-E1o fusions. As a result of this hexameric arrangement, the E1o and E2o active sites are poised at approximately 60 Å one to the other, with the oxoacid substrate and the acceptor CoASH getting access to them from different sides of the propeller ‘blade’ (Supplementary Fig. 6). Consistently, we could model CoASH, which was added to the cocrystallization mixture, as bound to the E2o

acceptor site (Fig. 2c), with the adenosine moiety adopting an equivalent pose to previously reported complexes with E2 enzymes^{30,31}.

Further inspection of the electron density maps revealed the presence of another 3'-phosphonucleotide, bound to the E1o domain in a pocket that was previously identified as the allosteric acetyl-CoA site in mycobacterial *KGD*²⁸ (Fig. 2d). We therefore modeled this ligand as acetyl-CoA, noting that supporting electron density for the pantothenate chain was also absent in *MskGD*_{Δ360} when crystals were soaked with millimolar concentrations of acetyl-CoA, in the absence of the 2-oxoglutarate substrate (PDB 2XTA; Supplementary Fig. 7)²⁸, suggesting a shared regulation mechanism between the two enzymes.

High-resolution cryo-EM studies of *OdhA*

To study the conformational changes triggered by substrates or allosteric regulators that might affect the domain reorganization, high-resolution single particle cryo-EM was employed for further structural characterization. After assessing the suitability of full-length *OdhA* samples for single particle analysis using negative staining EM (Supplementary Fig. 8), plunge-frozen samples were prepared at different protein concentrations in the presence of the oxoglutarate analog

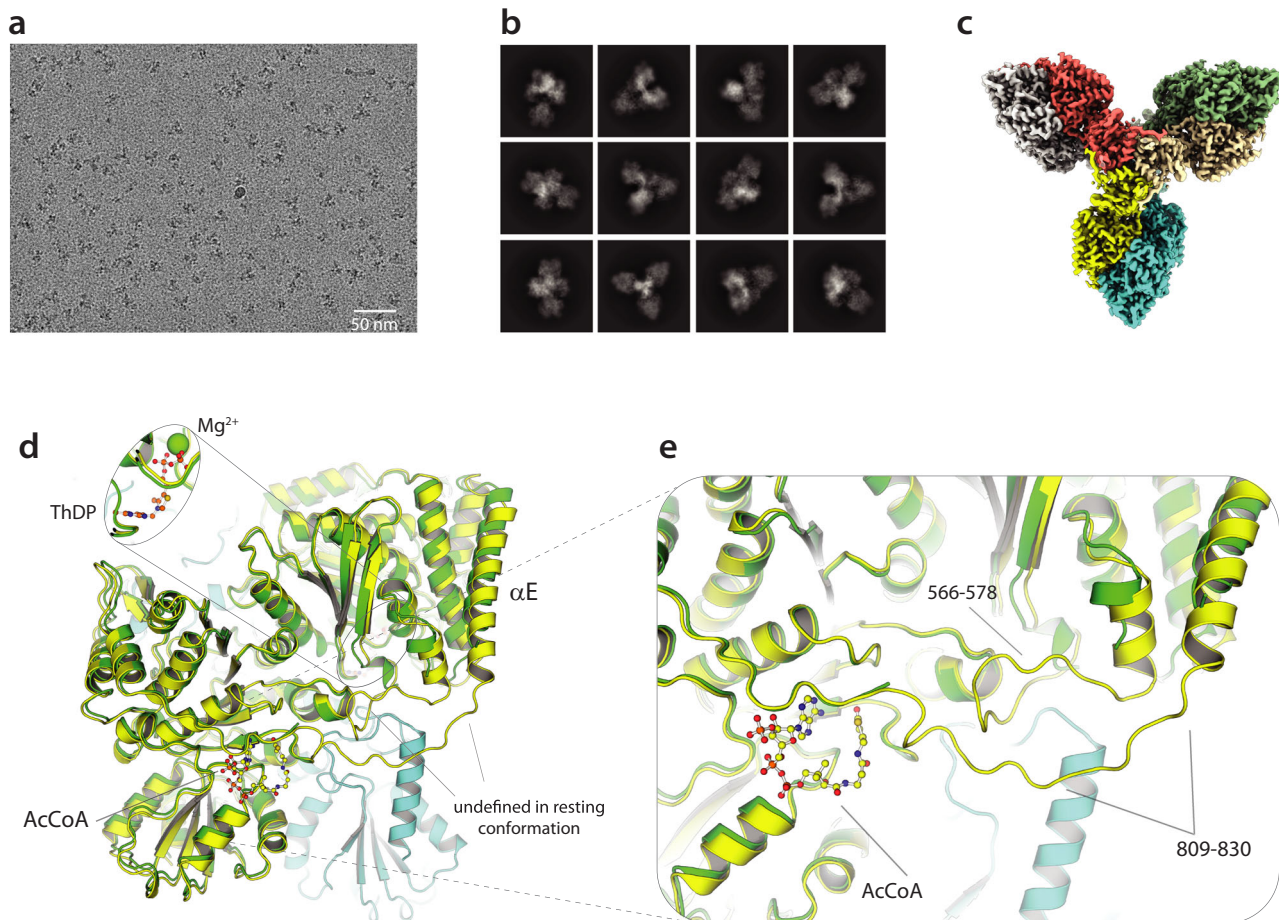


Fig. 3 | High-resolution single particle cryo-EM structure determination of OdhA. **a** Representative micrograph of an OdhA sample vitrified on an UltraAuFoil grid (Quantifoil), following motion correction and CTF estimation. **b** Representative 2D classes from the same dataset as in **a**. **c** Overall representation of the OdhA EM map at 2.2 Å resolution, showing the OdhA homohexamer (one color per chain). **d** Superimposition, focused on the E1o domain, of the OdhA Δ 97 model (green) to the OdhA model determined by single particle cryo-EM in the absence of added ligands (yellow/light blue). Loops that could not be traced in OdhA Δ 97 are indicated. Also, to be noted the different position of the α E external helix (see also Supplementary Fig. 12). **e** Zoomed view on the region most

concerned by the conformational change, from the resting conformation (observed for the OdhA Δ 97 crystal structure) to the active conformation observed by cryo-EM. Loops that become well defined in the active conformation are indicated, as well as the acetyl-CoA molecule observed in the allosteric E1o pocket in the OdhA model obtained by cryo-EM. An acetyl-CoA molecule bound in the same pocket was observed in all the OdhA complexes solved by single particle cryo-EM, except for the OdhA-OdhI complex. The OdhA Δ 97 model also presents a CoA ester (presumably acetyl-CoA) bound in the same pocket, although the lack of supporting electron density hindered tracing of the whole pantothenate chain (Fig. 2).

succinyl phosphonate (SP), previously shown to stabilize KGD³⁷. Single particle cryo-EM allowed us to get a first OdhA map at 3.4 Å resolution, following *ab initio* reconstruction and 3D refinement applying dihedral D3 symmetry. However, the narrow particle distribution precluded us to improve the map resolution. Raising OdhA concentration up to about 8 mg/ml and including 8 mM CHAPSO in the sample before plunge-freezing allowed a significant improvement of both the number of particles per micrograph and their orientation distribution (Fig. 3a/b), as reported in other cases³⁸, increasing the resolution of the reconstructed map up to 2.3 Å (Supplementary Fig. 9). A further improvement of the map up to 2.2 Å (Fig. 3c) was obtained by combining maps generated by local refinement of the two separate domains (Supplementary Fig. 9; Supplementary Movie 1). The same grid preparation strategy was then applied to other full-length OdhA samples, i.e. enzyme without added ligands, or preincubated with either CoASH or succinyl-CoA, leading to maps at comparable resolutions of 2.1–2.2 Å (Supplementary Fig. 10; Table 2). In all cases, the maps, which showed well-defined density for most side chains, allowed to trace the OdhA polypeptide chain unambiguously starting from residue Pro102, corresponding to the N-terminal boundary of the E2o domain, with excellent stereochemical parameters (Table 2). In

contrast, the full N-terminal OdhA segment, corresponding to the first hundred residues that include a predicted helical hairpin analogous to the one observed in the crystal structure of *MskGD* (Fig. 1b), could not be traced due to the lack of supporting density, confirming its high mobility in solution. The E1o active site at the dimer interface showed a clear density for ThDP-Mg²⁺ in all cases (Supplementary Fig. 11). In the case of the OdhA-SP complex, the phosphonate molecule, determined by surface plasmon resonance to bind OdhA with a K_D of $119 \pm 17 \mu\text{M}$, could be modeled as covalently linked to the reactive C2 carbon from the ThDP thiazolium ring (Supplementary Fig. 12). Such adduct, equivalent to the one generated upon cocrystallization of *MskGD* Δ 360 (PDB 6R29³⁷), provides an excellent mimic of the pre-decarboxylation complex and, in turn, of the incoming 2-oxoglutarate substrate (Supplementary Fig. 12).

Previous work on *MskGD* has shown the existence of two different conformational states of its E1o domain, i.e. a resting (or *early*) state *vs.* an activated (or *late*) state^{28,36}. The activated state was trapped following the addition of substrates and was associated to post-decarboxylation ThDP-bound intermediates deriving from either 2-oxoglutarate or 2-oxoadipate³⁶, or phosphonate analogs³⁷. In contrast to the crystallographic structure of OdhA Δ 97 which fits the resting

Table 2 | Cryo-EM data collection, refinement and validation statistics

Dataset	OdhA	OdhA-CoASH	OdhA-succinyl-CoA	OdhA-SP	OdhA-OdhI
Data collection and processing					
Grid type	UltrAuFoil300 mesh R1.2/1.3	UltrAuFoil300 mesh R1.2/1.3	UltrAuFoil300 mesh R1.2/1.3	Lacey 200mesh	Lacey 200mesh
Plunge freezer	Vitrobot	Vitrobot	Vitrobot	Vitrobot	Vitrobot
Microscope	Krios	Krios	Krios	Krios	Krios
Magnification	105000	105000	105000	105000	105000
Voltage (kV)	300	300	300	300	300
Energy filter(eV)	20	20	20	20	20
Camera	K3	K3	K3	K3	K3
Detector mode	Counted	Counted	Super-resolution	Counted	Counted
Electron exposure (e-/Å ²)	40	40	48	40	40
Defocus range (µm)	-0.8 to -2.0	-0.8 to -2.0	-0.8 to -2.0	-0.8 to -2.2	-0.8 to -2.2
Pixel size (Å)	0.86	0.86	0.84	0.86	0.86
Micrographs	13348	12202	11827	16647	19443
No. of fractions	40	40	50	60	40
Symmetry imposed	D3	D3	D3	D3	D3
Initial particle images (no.)	6571029	3392043	3827956	2599031	3177955
Final particle images (no.)	1474608	1849406	1074837	646352	958690
Map resolution (Å) ^a	2.17	2.17	2.07	2.26	2.29
FSC threshold	0.143	0.143	0.143	0.143	0.143
Map resolution range (Å)	1.9–4.4	1.9–4.5	1.9–4.7	2.0–4.6	2.0–6.0
Refinement and validation					
Model-map resolution (Å) ^b	2.3	2.2	2.2	2.3	2.3
FSC threshold	0.5	0.5	0.5	0.5	0.5
Map sharpening B factor (Å ²)	-84.4	-88.5	-74.2	-87.3	-93.3
Model composition					
No. Atoms (non-H)	52590	52878	54248	52656	55346
Protein residues	6714	6714	6726	6714	7110
Ligands	18	24	24	18	12
Water molecules	-	-	1280	-	-
Average B factors (Å ²)					
Protein	45.28	43.41	67.11	45.07	47.22
Ligands	56.18	57.52	83.72	56.28	123.89
R.m.s. deviations ^b					
Bond lengths (Å)	0.010	0.010	0.006	0.008	0.013
Bond angles (°)	1.247	1.229	1.032	1.121	1.810
Validation ^b					
MolProbity score	1.00	1.02	1.08	0.88	0.90
Clashscore	1.05	1.25	1.82	0.77	0.66
Poor rotamers (%)	0.42	0.31	0.53	0.11	0.21
Ramachandran plot ^b					
Favored (%)	96.82	97.02	97.26	97.24	96.87
Allowed (%)	3.18	2.97	2.74	2.67	3.13
Outliers (%)	0.00	0.01	0.00	0.09	0.00
PDB accession code	8P5T	8P5U	8P5V	8P5W	8P5X
EMDB accession code	EMD-17452	EMD-17453	EMD-17454	EMD-17455	EMD-17456

^aResolution estimates from cryoSPARC (version v3.2.0)⁵¹.

^bValues from MOLPROBITY⁵⁸ and the PHENIX⁵⁹ EM validation tools.

state, all our models refined on single particle EM maps adopt an activated conformational state of the E1o domain, even in the absence of added ligands. The state is indeed revealed by the shifts in the loops 566–579 as well as 809–836, that could be traced in the EM structures but were mostly unstructured in the OdhA_{Δ97} crystal structure (Fig. 3d/e; Supplementary Fig. 13)^{28,36}. However, all the OdhA cryo-EM datasets, including those corresponding to complexes with CoASH, succinyl-

CoA and SP, show an acetyl-CoA molecule bound to E1o allosteric site which could be positioned unambiguously (Fig. 3d/e; Supplementary Fig. 14). The presence of a bound acetyl-CoA activator, most likely acquired following heterologous overexpression of the enzyme in *E. coli*, may therefore explain the observed OdhA activated conformation through a mechanism that involves the stabilization of the loop 809–836 in its extended form (Supplementary Fig. 14), promoting, in turn,

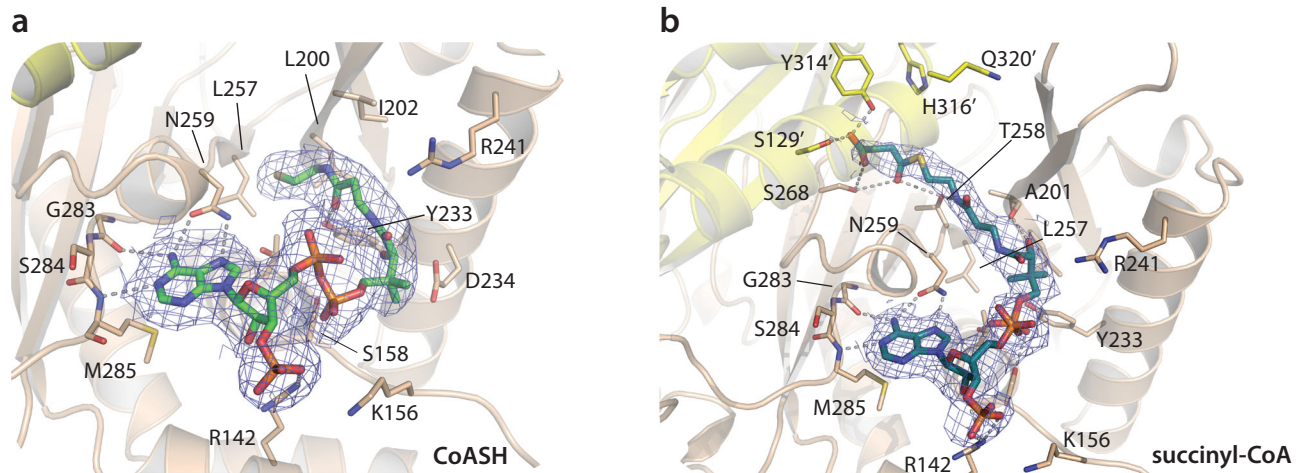


Fig. 4 | Substrate and product binding in the OdhA E2o (succinyltransferase) active site. Cartoon representation of CoASH (a) vs. succinyl-CoA (b) binding in the OdhA E2o active site, as determined by high-resolution single particle cryo-EM. To note, the terminal sulfhydryl group of CoASH does not reach the catalytic center (identifiable by the His316/Gln320 dyad), but is accommodated in a mostly hydrophobic pocket defined by Leu200, Ile202, and Leu257, with the hydroxyl

group of Tyr233 acting as a hydrogen bond donor to the terminal carbonyl oxygen of CoASH. This binding orientation, although not identical, corresponds to the ‘OUT’ conformation originally observed in the ternary complex of *A. vinelandii* E2p with CoASH and free lipoamide (PDB 1EAB; Supplementary Fig. 15). Blue meshes corresponds to the EM map for the ligands, contoured at the 3.5 σ level.

the activated conformation²⁸. This hypothesis is supported by previous observations showing that acetyl-CoA binding to *MsKGD* contributed to stabilize the activated conformation²⁸, as well as by steady-state kinetic and spectroscopy studies that concluded that acetyl-CoA acts as a mixed V and K type allosteric activator on mycobacterial KGD³⁹.

The ensemble of high-resolution OdhA single-particle cryo-EM complexes provides insights into the functionality of the E2o succinyltransferase domain. First, the OdhA-CoASH complex shows the bound CoASH with the pantothenate chain not entering the active site, but with the terminal, reactive sulphhydryl group accommodated in the mostly hydrophobic pocket defined by Leu200, Ala201, Thr258 and the side chains of Ile202 and Leu257 (Fig. 4a). Such CoASH binding mode is close to the previously reported ‘out’ conformation of CoASH in the non-proficient, ternary complex of *Azotobacter vinelandii* E2p (PDB 1EAB) (Supplementary Fig. 15), where it was proposed as a mechanism to protect the reactive sulphhydryl group from oxidation³¹. In contrast, succinyl-CoA binds to the same domain with its 2-phosphoadenosine moiety superimposable to the one observed for CoASH, but the pantetheine arm directed towards the E2o active site. Noteworthy, its pose is overall very close to the one shown by CoASH in its ternary complex with lipoamide in AceF (E2p) from *C. glutamicum*³⁰ (Supplementary Fig. 16). Specifically, the sulfur atom is positioned at 5 Å from the NE2 nitrogen of the catalytic His316 belonging to the neighboring subunit (Fig. 4b), a distance compatible with the proposed catalytic mechanism³¹, while the terminal carboxyl group from the succinyl moiety is stabilized by hydrogen bonds with Ser129 and Tyr314, also provided by the adjacent subunit. At the same time, the ketone oxygen acts as H-bond acceptor to Thr258 and Ser268 (Fig. 4b; Supplementary Fig. 15/16). The observed succinyl-CoA binding mode agrees with mutagenesis data pointing to a catalytic role for His316 and Gln320, and suggesting Thr258 as involved in CoA binding (Supplementary Fig. 16)²⁶. It is worth noting that both Ser129 and Tyr314 are conserved among OdhA orthologues (Supplementary Fig. 17) as well as in structurally characterized E2o enzymes, but not in E2s with different substrate specificity (Supplementary Fig. 5), consistently with the observed role of these residues in stabilizing the terminal carboxyl group from the succinyl moiety. Our snapshots therefore suggest them as one of

the structural features that may contribute to provide substrate selectivity to E2 enzymes.

FHA regulation: specific interactions for a conserved inhibition mechanism

By preincubating purified OdhA with an excess OdhI and passing the sample through size exclusion chromatography prior to grid preparation, we were also able to obtain a single particle reconstruction of a full OdhA-OdhI complex at 2.3 Å resolution (Supplementary Movie 2). The overall structure is very similar to that of the homologous *MsKGD-GarA* complex (Figs. 1 and 5a), with OdhI molecules binding, through their FHA domains (traceable for residues Glu40-Ala142), to the OdhA E1o domain with a 1:1 stoichiometry. In contrast to the other single particle EM structures, OdhA adopts here the resting conformation, equivalent to the one observed in the crystal structure of OdhA_{Δ97} and consistently with structural and kinetic observations on mycobacterial KGD, both indicating that GarA binding stabilized this enzyme conformation^{32,39}. Moreover, no ligand bound to the OdhA acetyl-CoA allosteric site could be detected in this complex, suggesting that bound acetyl-CoA may have been lost because of OdhI binding, further confirming the link between the presence of the activator and the conformational state of the enzyme.

Interactions with OdhA involve the tips of both OdhI FHA anti-parallel β -sheets: one anchors firmly to the OdhA loop Leu591-Glu598, which connects two antiparallel β -strands, while the tip of the other OdhI β -sheet binds the OdhA α -helices Gln480-Lys503 and Asn786-Asn805 (α E) (Fig. 5b). The interactions of the former involve the OdhI positively charged Arg53, Lys132 and Arg134 side chains which bind, through a network of hydrogen bonds, to main chain carbonyl oxygens of the OdhA 591-598 loop (Fig. 5b), in a similar way as in the *MsKGD-GarA* complex³². However, the interactions between OdhI and the OdhA helix α E, which is a landmark of the enzyme activation state^{28,36}, show a few significant differences when compared to the mycobacterial complex. The α E helix could only be traced till residue 805 in OdhA, and it shows a 30° kink towards OdhI at its N-terminal tip (Fig. 5c). Most notably, no hydrogen bond was observed between the phosphomimetic residue Asp795 in OdhA and OdhI Ser86, in contrast to structural observations on the *GarA-MsKGD* complex^{32,40} but consistently with site-directed mutagenesis on OdhI, which pointed to

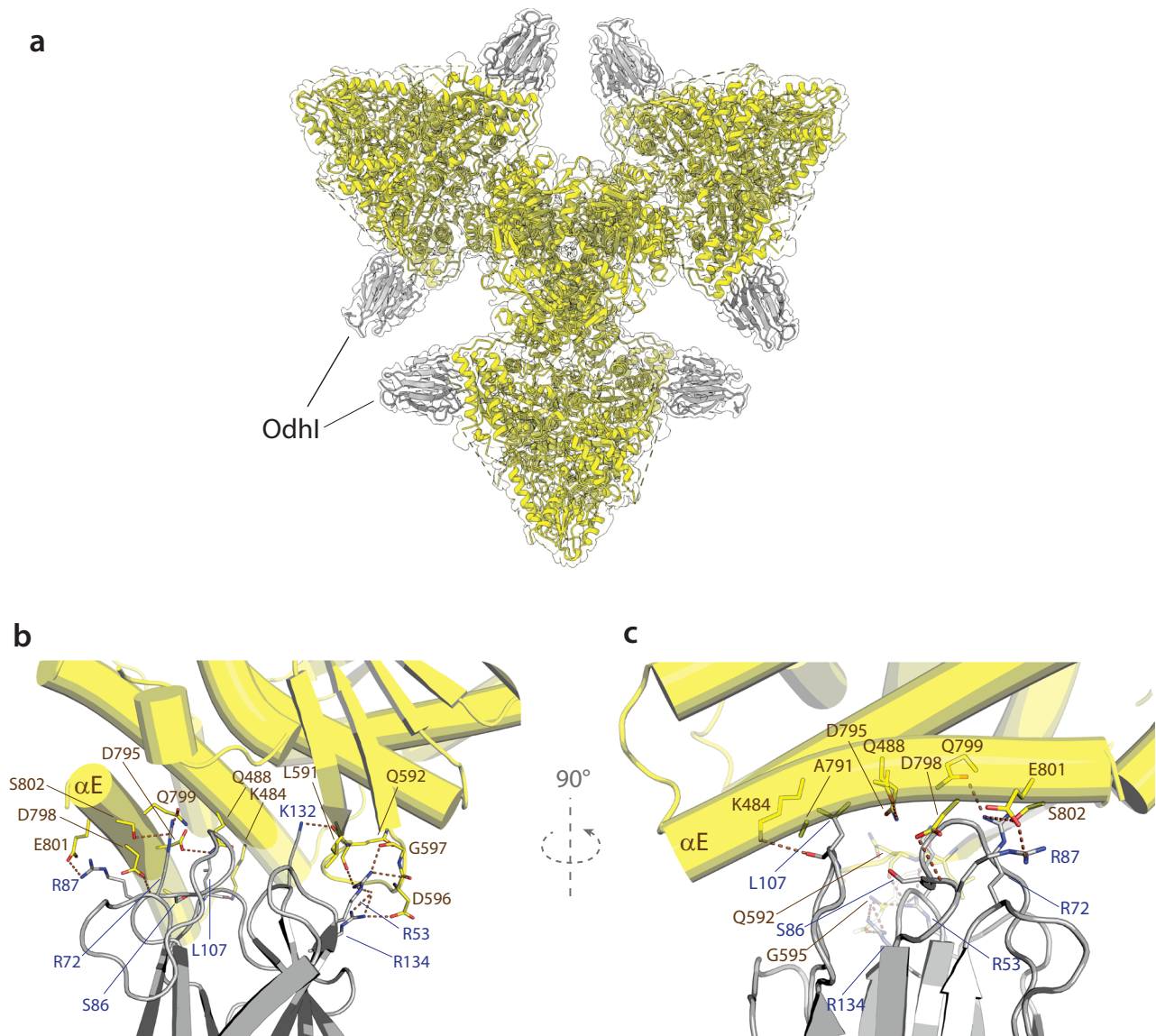


Fig. 5 | Single particle cryo-EM structure of the OdhA-OdhI complex.

a Visualization of the OdhA-OdhI complex fit in the corresponding single particle EM map at 2.3 Å resolution. **b** Detailed view of the interactions between OdhA (yellow) and OdhI FHA domain (gray), with involved residues depicted as sticks.

Dashed lines indicate hydrogen bonds and salt bridges. OdhA helices are depicted as cylinders. **c** Rotated view of the OdhA-OdhI interactions. αE refers to the OdhA α-helix Ser785-Asn805, following the original *MskGD* nomenclature.

Ser86 as dispensable for binding⁴¹. Accordingly, the binding affinity of the GarA S95A variant for *MskGD* was comparable to the wild-type³².

A negatively charged side chain from Asp798, adjacent to Asp795 on the αE outside surface (instead of a glycine in *MskGD* and other orthologues; Supplementary Fig. 17), exists additionally in OdhA within hydrogen-bonding distance to the main chain amino group of OdhI Arg87. The side chain of the same Arg87, in turn, is involved in a salt bridge with OdhA Glu801 (Fig. 5b/c), pointing to a key role of this residue in the OdhI-OdhA interaction. In agreement with these observations, mutations leading to the substitution of OdhI Arg87 to either proline or alanine have been isolated in suppressor mutants of a *glnX* gene deletion in *C. glutamicum*, where the impaired OdhA inhibition overcomes the accumulation of unphosphorylated OdhI⁴². In the same work, a missense mutation involving OdhI Leu107 was also isolated in a mutant strain bearing the same suppressor phenotype⁴², consistently with this residue being located at the OdhA-OdhI interface. Leu107 is indeed involved in van der Waals interactions with OdhA Ala791 and the side chains of both Lys484 and Gln488 (Fig. 5c; Supplementary Fig. 18), the substitution of which was shown to impair

the *MskGD*-GarA interaction³². Overall, the OdhI relative position is shifted approximately 2 Å aside from OdhA when compared to GarA in the corresponding mycobacterial *MskGD*-GarA complex (distance calculated as the RMSD over the ensemble of Cα; Supplementary Fig. 18), resulting in a -5 Å distance between the OdhI Ser86 OG oxygen and the carboxyl group of OdhA Asp795. An additional, distinct intermolecular interaction in OdhA-OdhI is due to the presence of a serine residue at OdhA position 802, still positioned on the αE helix and making a hydrogen bond to OdhI Arg72 (Fig. 5b), while an arginine is found at the corresponding position in *MskGD*, as well as in other OdhA-like enzymes (Supplementary Fig. 17). Replacing this residue by an alanine was indeed found to decrease 6.25-fold the K_i of GarA for KGD³². Overall, despite a similar molecular surface occluded on the FHA domain upon the interaction with either *MskGD* or OdhA (around 950 Å²), and a conserved inhibition mechanism, our high resolution cryo-EM model provides a molecular view to explain the 100-fold lower K_D of OdhI on OdhA⁴¹ *vs.* GarA on *MskGD*, as determined by surface plasmon resonance³².

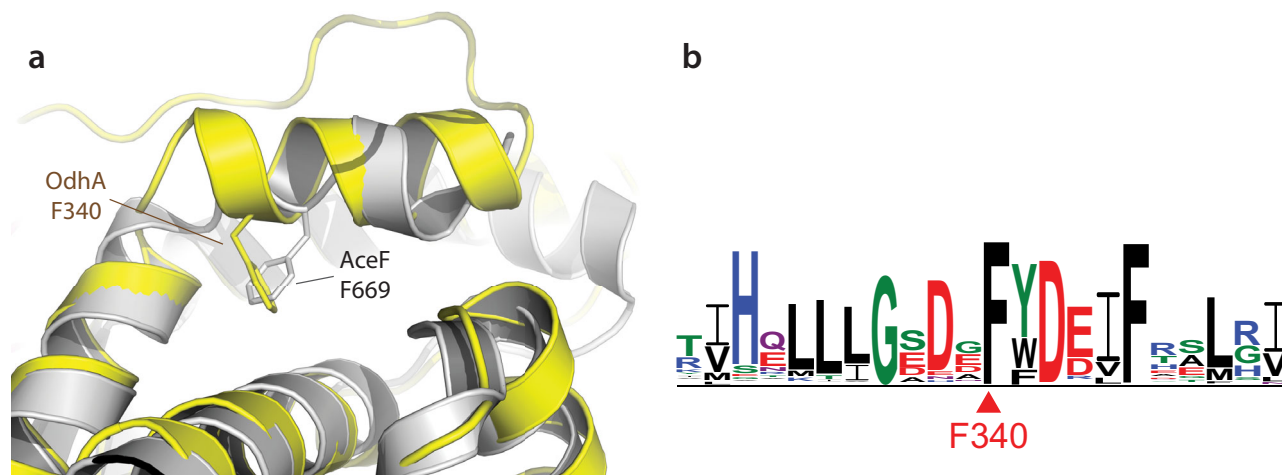


Fig. 6 | The E2o/E1o domain boundary in OdhA. **a** Superimposition of the E2o domain of OdhA (yellow) to the catalytic domain of *C. glutamicum* E2p (AceF; gray, PDB 6ZZ1²⁰). Focus is on the amphipathic helix that marks the C-terminal boundary of the OdhA E2o domain, which shows the same relative position as the C-terminal helix in AceF. To note the presence of a structurally conserved phenylalanine residue (indicated) that, in both proteins, contributes to maintain the helix relative

orientation through intramolecular interactions. Such orientation was shown to be key to the loss of high-order oligomerisation in actinobacterial E2p enzymes. **b** Sequence logo derived from a multiple sequence alignment of OdhA orthologues from representative members of the Actinobacteria phylum (see Supplementary Fig. 17). The logo is here limited to the OdhA residues surrounding the conserved Phe340.

Interactions between the two catalytic centers

The homohexameric arrangement of OdhA challenges current paradigms about the composition and protein-protein interactions within PDH and ODH complexes and raises questions regarding the coordination of the different catalytic activities carried out by the same polypeptide. We previously reported how the E2o domain contributes to regulate E1o activity in *MskGD* by restraining protein motions involved in the transition from the resting to the active state²⁸. An arginine residue (Arg781) situated on the loop preceding the α E helix was indeed shown to mediate contacts with the E2 domain, and the analysis of available sequences of OdhA homologs from Actinobacteria shows the conservation of this residue (Supplementary Fig. 17). In the resting state OdhA_{Δ97} crystal structure, Arg781 hydrogen bonds to the main chain oxygens of Arg151 and Thr152, but these interactions are not observed in the EM models (including the OdhA-OdhI complex), where the distance of the guanidium group to the Arg151 carbonyl oxygen is around 7 Å. A salt bridge in between Asp777 (helix α E) and Arg153 from the E2o domain is observed instead (Supplementary Fig. 19). Intrigued by these differences that suggest interdomain mobility, we performed 3D variability analysis⁴³ on all our EM datasets. The results indicate indeed twisting of the E1o domains around the hexamer plane, as well as tilting movements of the longitudinal axes of the same E1o domains, which deviate from their average position on the three-fold axis of the hexamer (Supplementary Movie 3), reinforcing the hypothesis that interdomain flexibility is a major contributor to protein dynamics, which, by remodeling the contact network, may contribute to enzyme regulation.

The homohexameric OdhA architecture also provides a further example of conservation of structural motifs at the domain interfaces. We showed recently how actinobacterial E2p enzymes lose their typical high molecular weight oligomerization due to a specific 3-residue insertion at their C-terminus, and as a consequence they are reduced to their minimal catalytic homotrimeric state³⁰. Specifically, the insertion makes the terminal 3_{10} helix, involved in symmetric trimer-trimer interactions, to deviate from its position making intramolecular contacts instead. It is worth noting that a similar situation is observed at the E2o-E1o interface in OdhA, where the C-terminal amphipathic α -helix from the E2o domain adopts a conformation substantially equivalent to the one observed in AceF (Fig. 6a), its internal face being held against helix α 3 from the same domain (OdhA residues Phe159-

Ala173), mostly by hydrophobic interactions. Moreover, a phenylalanine residue (Phe340 in OdhA) occupies a structurally equivalent position to Phe669 in AceF (Fig. 6a), shown to be a key conserved residue of the 3-amino acid insertion in actinobacterial E2. Likewise, as observed in AceF, the Phe340 OdhA side chain contributes directly to fill the hydrophobic pocket which, in canonical E2 enzymes, would accommodate the incoming C-terminal 3_{10} helix from the facing trimer, in the so-called ‘knobs and socket’ interaction. Consistently, sequence alignment of OdhA orthologues shows the conservation of the phenylalanine residue (Fig. 6b; Supplementary Fig. 17), in agreement with previous considerations³⁰ and thus confirming the role of the phenylalanine-containing insertion (PCI) as a structural motif in actinobacterial E2 enzymes.

Discussion

2-oxoacid dehydrogenase complexes have long made a textbook example of megadalton-sized, universally conserved multienzymatic machineries, each dedicated to specific, yet conserved, three-step reactions located at the core of central metabolism. These complexes have, so far, been thought to be centered around large hollow cores composed of multiple copies of specific E2 (acyltransferase) enzymes, which, through long and flexible linkers that bear lipoyl and interaction domains, anchor the E1 (ThDP-dependent decarboxylases) and E3 (lipoamide dehydrogenase) components on the outside surface. Despite the first evidence of such architecture dates back to pioneering investigations in the sixties^{7,8}, the inherent flexibility of the E2 interdomain linkers and the transient nature of some of the protein-protein interactions has long hampered a detailed understanding of such complexes. Even their stoichiometry, including in well-studied model organisms like *E. coli*, has long been a matter of debate. Thanks to methodological advances in single particle EM, and to the application of integrative approaches, the last couple of years have however seen significant advances in the field, ranging from the composition of eukaryotic E2p and E2o cores^{22–24,44–46}, to snapshots of protein interactions and dihydrolipoyl-lysine entering the E2 active site^{2,21,24,47}. None of the aforementioned studies, however, dealt with complexes deviating significantly from the well-established general architecture of oxoacid dehydrogenases. Here, by a combination of high-resolution X-ray crystallography and single particle EM analysis, we show how evolution, through shuffling and fusion of domains, combined fully

98-1221) was also generated by Genscript from pET-28a-TEV/OdhA. The *C. glutamicum* ATCC13032 *aceE* (Uniprot accession no. Q8NNF6, residues 1-922) and *lpd* (Uniprot accession no. Q8NTEI, residues 1-469) open reading frames were amplified by PCR (Supplementary Table 2) and inserted, by restriction-free cloning⁴⁹, into the pET-32a derived pT7 expression vector providing a TEV cleavage site at the 5' end of the target gene⁵⁰. Constructs were verified by DNA sequencing.

Protein purification

Full-length *MskGD* was overexpressed in *E. coli* BL21(DE3)pLysS and purified as previously described²⁸. Both OdhA expression constructs (pET-28a-TEV/OdhA and pET-28a-TEV/OdhA_{Δ97}) were introduced into *E. coli* BL21(DE3), and protein expression achieved following the same autoinduction scheme⁵¹. Recombinant proteins were also purified following the same protocol. After an overnight incubation at 30 °C in 2YT-based autoinduction medium containing 50 μg/ml kanamycin, cells were harvested and frozen at -80 °C. Cell pellets were resuspended in 50 ml lysis buffer (25 mM Tris pH 8.5, 300 mM NaCl, 25 mM imidazole, supplemented with benzonase and EDTA-free protease inhibitor cocktails (Roche)) at 4 °C, and lysed by a CF2 cell disruptor (Constant Systems Ltd.). The lysate was centrifuged for one hour at 13,000 ×g at 4 °C. The clear supernatant was loaded onto a Ni-NTA affinity chromatography column (1 ml HisTrap FF crude, Cytiva), and his-tagged proteins were eluted with a linear gradient of buffer B (25 mM Tris pH 8.5, 300 mM NaCl, 400 mM imidazole). The eluted fractions containing the protein of interest were pooled and TEV protease, produced as described⁵², was added at 1:30 w/w ratio. The sample was then dialyzed overnight at 4 °C against 20 mM HEPES pH 7.5, 500 mM NaCl, 1 mM DTT using 'SnakeSkin' dialysis tubing with a 7 kDa molecular weight cut-off (ThermoFisher). His₆-tagged cleavage products as well as TEV protease were removed with Ni-NTA agarose resin (Qiagen) on gravity flow disposable plastic columns. The sample was then concentrated and loaded onto a Sephacryl S-400 HR 16/60 size exclusion (SEC) column (Cytiva) pre-equilibrated in 20 mM HEPES pH 7.5, 500 mM NaCl (20 mM HEPES pH 7.5, 300 mM NaCl for OdhA_{Δ97}). Fractions corresponding to the OdhA peak were checked on SDS-PAGE (Supplementary Fig. 20), pooled and concentrated. The resulting sample was either used directly for cryo-EM grid preparation, or flash-frozen in small aliquots in liquid nitrogen and stored at -80 °C.

OdhI was overexpressed by autoinduction in *E. coli* BL21(DE3) grown in the same 2YT-based medium as OdhA, but overnight culture at 14 °C. The purification also followed the protocol above, but size-exclusion chromatography was performed on a HiLoad Superdex 75 16/60 column run in 25 mM Tris-HCl pH 8.5, 150 mM NaCl. Likewise, Lpd (E3) was also overexpressed by autoinduction in 2YT-based medium supplemented with 50 μg/ml carbenicillin, with overnight culture at 18 °C; the protein was purified following the same steps, except for size-exclusion chromatography performed on a HiLoad Superdex 200 16/60 column run in 50 mM Tris-HCl pH 8.5, 150 mM NaCl, 5% glycerol. AceE (E1p) was overexpressed, in *E. coli* BL21(DE3) grown in LB medium containing 50 μg/ml carbenicillin, by the addition of 0.5 mM IPTG at the optical density of ~0.6 (600 nm), followed by 18 h growth at 18 °C. The recombinant protein was purified following the same protocol as OdhA, with the size-exclusion chromatography step performed on Sephacryl S-400 HR 16/60 equilibrated in 50 mM Tris-HCl pH 8.5, 150 mM NaCl, 5% glycerol. *C. glutamicum* full-length AceF (E2p) and *M. smegmatis* GarA were expressed and purified as previously described^{30,32}.

Oxidative decarboxylation and 2-oxoacid dehydrogenase assays

Oxidative decarboxylation activity of OdhA was determined by measuring 2,6-dichlorophenolindophenol (DCPIP) reduction at 600 nm and 25 °C²⁶. The reaction medium contained 0.1 M KH₂PO₄ pH 7.0, 1 mM ThDP, 1 mM MgCl₂, 0.25 mM DCPIP, and 1 mM 2-oxoglutarate.

The reaction was started by addition of reaction medium to a well containing 9 μg of OdhA to the final volume 200 μl. Blank reaction rate was measured in the reaction medium omitting 2-oxo acid. The extinction coefficient of DCPIP used for calculations is 20.6 mM⁻¹cm⁻¹. 2-oxoacid dehydrogenase activity (PDH or ODH) was determined in conditions adapted from previous reports^{26,27}. The assay medium contained 50 mM TES buffer pH 7.7, 10 mM MgCl₂, 3 mM L-cysteine, 0.9 mM TPP, 50 μM chlorpromazine, 2 mM NAD⁺, 0.2 mM coenzyme A, 10% glycerol and either 1.5 mM pyruvate or 1.5 mM 2-oxoglutarate to measure PDH or ODH activity, respectively. To achieve an approximately equimolar ratio while accounting for the presumed oligomeric state of each enzyme, 414.8 μg of OdhA, 105.6 μg of AceE, 109.8 μg of AceF, and 52.2 μg of Lpd were mixed at final concentration 11.2 mg/ml. Before activity measurements, the mixture was incubated on ice for at least 30 min. Reactions were started by adding the reaction medium to the protein mixture (10–40 μl) in a final volume of 200 μl, and were followed by NADH absorbance at 340 nm at 30 °C, using an Infinite M1000Pro reader (Tecan). Blank reaction rate was measured in the reaction medium omitting the 2-oxoacid substrate. Extinction coefficient of NADH used for calculations is 6.22 mM⁻¹cm⁻¹.

Crystallization

Initial crystallization screenings were performed at 18 °C by vapor diffusion in 96-well plates, according to established protocols at the Crystallography Core Facility of the Institut Pasteur⁵³. Crystals of the OdhA_{Δ97}-CoASH complex were obtained from a 26 mg/ml OdhA_{Δ97} solution, supplemented with 5 mM CoASH and crystallized in 0.1 M HEPES-NaOH pH 7.5, 5% (w/v) PEG 4000, 30% (v/v) methylpentanediol (MPD) by the sitting drop method; for the *MskGD*-GarA complex, crystals were obtained from a 10 mg/ml *MskGD* solution supplemented with 2 mM ThDP, 5 mM MgCl₂ and *M. smegmatis* GarA (1:1 molar ratio), and crystallized, through the hanging drop method, in 0.1 M bicine pH 8.0, 30% (v/v) PEG550MME, 0.2 M NaCl.

X-ray diffraction data collection and structure solution

Diffraction datasets were acquired either on the beamline ID30A-3 at the ESRF synchrotron (Grenoble, France), or on the beamline Proxima-1 at the SOLEIL synchrotron (Saint-Aubin, France). Data integration and scaling were performed with *autoPROC*⁵⁴, applying anisotropic scaling via *STARANSO*. Structures were solved by molecular replacement through the program *PHASER*⁵⁵, using the previously released coordinates of the *MskGD*_{Δ115} homodimer (PDB 2XT6²⁸) as the search model for both datasets (OdhA_{Δ97}-CoA and *MskGD*:GarA). *M. smegmatis* GarA coordinates were retrieved from the previously published *MskGD*_{Δ360}:GarA complex (pdb 6I2Q³²). Manual model rebuilding and ligand placement in electron density maps was entirely performed with *COOT*⁵⁶. Refinement was carried out with *BUSTER*, applying local structure similarity restraints for non-crystallography symmetry (NCS)⁵⁷ where appropriate, and a Translation-Libration-Screw (TLS) model. Chemical dictionaries for ligands were generated with the Grade server (<http://grade.globalphasing.org>). Validation of models was performed with *MOLPROBITY*⁵⁸ and the validation tools in *PHENIX*⁵⁹. Data collection, refinement and model statistics are indicated in Table 1. Software was distributed by the SBGrid consortium⁶⁰.

Negative staining EM

5 μl of purified OdhA sample, at concentrations of either 0.05 mg/ml or 0.01 mg/ml, were applied over 400-mesh copper carbon coated grids (Electron Microscopy Sciences) that were previously glow discharged at 2 mA for 20 s. Grids were washed twice in 10 μl water for 40 s, then stained in a 2% uranyl acetate solution (twice for 40 s). Grids were then blotted using a Whatman 1 filter paper and air dried for 5 min. Micrographs were acquired on a Tecnai T12 transmission electron microscope (ThermoScientific), operating at 120 kV, at magnification rates comprised between 30,000× and 180,000×.

Cryo-EM sample preparation and data collection

OdhA samples were vitrified at a concentration of 12.0 mg/ml (protein without ligands, incubated with CoASH or succinyl-CoA), or 8.0 mg/ml for the OdhA-SP complex. The OdhA-OdhI complex was prepared by incubating a mixture of the two proteins at molar ratio 1:10, which was then subjected to size-exclusion chromatography on a Superose 6 increase 5/150 GL column (Cytiva), run in 20 mM Hepes pH 7.5, 500 mM NaCl. UltrAuFoil R1.2/1.3 300 mesh gold grids (Quantifoil) were used for OdhA alone, OdhA-CoASH or OdhA-succinyl-CoA, while OdhA-SP and OdhA-OdhI were vitrified on Lacey carbon 200 mesh grids (Electron Microscopy Sciences). Grids were glow discharged for 25 s at 50 W (UltrAuFoil R1.2/1.3) or 10 s at 5 W (Lacey) under 35.0 sccm Ar, with a Solarus II plasma cleaner (Gatan). Vitrification was carried out using a Vitrobot Mark IV (ThermoScientific), applying 3 μ l of protein sample to the grid surface at a temperature of 4 °C and humidity level of 100%. Grids were then blotted (during 4 s at blot force 0 for Lacey grids, blot force 2 for UltrAuFoil R1.2/1.3 grids) and plunge-frozen into liquid ethane. Data from all samples but OdhA-succinyl-CoA were collected at the Nanoimaging Core facility in Institut Pasteur on a Titan Krios electron microscope (ThermoScientific), operated at 300 kV and equipped with a K3 direct electron detector (Gatan) operating in counted mode. The OdhA-succinyl-CoA dataset was instead collected on a Titan Krios microscope located at the ESRF (Grenoble, France), also running at 300 kV and equipped by a K3 detector operating in the counted super-resolution mode⁶¹. The software EPU (ThermoScientific) was used to pilot data collection in all cases. A summary of data collection and model refinement parameters is reported in Table 2.

Single particle analysis of cryo-EM data

All single particle cryo-EM datasets were processed through cryoSPARC version 3.2⁶². Motion correction was performed using full-frame motion correction and CTF estimation were performed using patch CTF estimation. Using the curate exposure feature, 12666 out of 13348 for OdhA alone, 7996 out of 12202 for OdhA-CoASH, 8796 out of 11827 for OdhA-succinyl-CoA, 15025 out of 16647 for OdhA-SP, and 14842 out of 19443 for OdhA-OdhI complex were selected for further analysis. A first round of 'blob particle picking' was performed, and after 2D classification, the most populated classes were selected for template-based particle picking against a dataset containing the selected micrographs. Particles were extracted applying a box size of 384 Å, except for the OdhA-SP sample for which the box size was set at 448 Å. The extracted particles were cleaned using the 'inspect pick' function of Cryosparc and several rounds of 2D classification with selection of higher resolution classes were applied, selecting classes corresponding to a complete, hexamer shape of OdhA in different orientations. The selected particles were used, after local motion correction, to build an ab-initio model and non-uniform 3D refinement applying D3 symmetry, while optimizing per-particle defocus and per-group CTF parameters. For all datasets, local refinement was performed with a soft mask covering the OdhA E1o domain dimer. A composite map including the three OdhA E1o dimers was generated by the 'combine focused maps' tool in PHENIX (v. 1.20-4459-000)⁵⁹.

Single particle EM model building and refinement

OdhA coordinates obtained from X-ray crystallography were fitted into the corresponding cryo-EM density maps using UCSF Chimera (v1.13.1)⁶³. For the OdhA-OdhI complex, *C. glutamicum* OdhI coordinates were retrieved from the available crystal structure (pdb 4QCJ⁶⁴). Following a first round of rigid-body fitting of the E2o and E1o OdhA domains, and OdhI were appropriate, the models were improved by iterative rounds of restrained real-space refinement in PHENIX, and alternating rounds of model building with manual adjustment in COOT and further model refinement through the Servalcat pipeline⁶⁵ in the CCP-EM suite⁶⁶. Model validations were performed using the specific

tools in the PHENIX and CCP-EM suites. Figures were prepared using UCSF ChimeraX v.1.3⁶⁷, and PyMOL v. 2.5.4⁶⁸, distributed by the SBGrid consortium⁶⁰.

Surface plasmon resonance binding assay

Experiments were performed using a Biacore T200 instrument (Cytiva) and NTA sensorchips equilibrated at 25 °C in OdhA storage buffer (20 mM Hepes pH 7.5, 500 mM NaCl), complemented with 100 μ M EDTA and 0.2 mg/ml BSA. Two flow cells of the chip were first activated by running a 1 mM NiCl₂ solution for 2 min at 5 μ l/min, and loaded with OdhA-His₆ (200 μ g/ml) for 10 min at 5 μ l/min, reaching densities of 8800–10,000 resonance units (RU, \approx pg/mm²). 5 concentrations of SP were then injected sequentially in single cycle kinetics mode at 30 μ l/min for 2 min each, followed by a 2 min buffer wash to monitor the dissociation of the OdhA-SP transient complex. The sensorchip was finally fully regenerated by injecting 0.5 M EDTA, 0.1% SDS twice for 2 min at 5 μ l/min, allowing it to be reused for a new experimental cycle. Sensorgrams were processed using the BiaEvaluation software. The concentration-dependence of steady-state SPR signals (Req) was analyzed using the following equation: Req = Rmax * C/(K_D + C), where C is the SP concentration and Rmax the fitted maximal SPR signal at infinite SP concentration.

Analytical ultracentrifugation

Sedimentation velocity (SV) analytical ultracentrifugation assays were performed using a Beckman Coulter ProteomeLab XL-I analytical ultracentrifuge equipped with UV-Vis absorbance and Raleigh interference detection systems, using an 8-hole Beckman An-50 Ti rotor at 20 °C. Experiments were performed at 30,000 rpm. Seven concentrations (from 4 mg/ml to 0.0625 mg/ml, serial two-fold dilutions) were prepared for this experiment in the OdhA buffer (20 mM Hepes pH 7.5, 500 mM NaCl) and loaded into analytical ultracentrifugation cells. During the run, SV was followed by measuring absorbance at 280 nm for sample with concentration from 4 mg/ml to 0.25 mg/ml and at 225 nm for sample with concentration at 0.125 mg/ml and 0.0625 mg/ml. The software SEDFIT v. 15.01⁶⁹ was used to calculate the sedimentation coefficient distribution C(s), then corrected to standard conditions to get the final standard values. Coefficients were plotted as a function of the different concentrations and an extrapolation to zero concentration was made to obtain the standard value for the main oligomer. From these values, molecular mass and friction ratio were obtained.

Protein sequence analyses

Sequence analyses were carried out on a database representing all Actinobacteria diversity present at the National Center for Biotechnology (NCBI) as of February 2021, containing 133 taxa (five species per class). To identify OdhA homologs, the jackhmmer tool from the HMMER package (v3.3.2)⁷⁰ was employed, using the GenBank⁷¹ sequence BAB98522.1 as the query. The hits were aligned with mafft (v7.475)⁷² accurate option L-INS-I. The MSA was manually curated, removing sequences that did not align. A sequence logo of OdhA was created based on the MSA through the online tool WebLogo3⁷³. The secondary structure of protein OdhA was mapped on the MSA using the online tool ESPript⁷⁴.

Reporting summary

Further information on research design is available in the Nature Portfolio Reporting Summary linked to this article.

Data availability

Atomic models described in this study, accompanied by the corresponding structure factors (for X-ray crystallographic structures) and maps (for single particle cryo-EM) have been deposited to the Protein Data Bank (PDB) / Electron Microscopy Data Bank (EMDB), under the

following accession codes: MsKGD-GarA (crystal structure), PDB 8P5R; OdhA₉₇ (crystal structure), PDB 8P5S; OdhA (cryo-EM structure with no added ligands), PDB 8P5T / EMD-17452; OdhA-CoASH, PDB 8P5U / EMD-17453; OdhA-succinyl-CoA, PDB 8P5V / EMD-17454 (raw data available at [<https://doi.org/10.1515/ESRF-ES-514136397>]); OdhA-SP, PDB 8P5W / EMD-17455; OdhA-OdhI complex, PDB 8P5X / EMD-17456. Previously published structural models cited in the paper include the PDB entries 1EAB, 2XTA, 2XT6, 4QCJ, 6I2Q, 6R29, 6ZZI. Source data are provided as a source data file, containing raw data relative to enzymatic activity measurements, analytical ultracentrifugation (Supplementary Fig. 2), SPR experiments (Supplementary Fig. 12b/c) and OdhA size-exclusion chromatography profile (Supplementary Fig. 20) are provided as a Source Data file with this paper. Source data are provided with this paper.

References

- Perham, R. N. Swinging arms and swinging domains in multi-functional enzymes: catalytic machines for multistep reactions. *Annu. Rev. Biochem.* **69**, 961–1004 (2000).
- Nemeria, N. S. et al. Functional versatility of the human 2-oxoadipate dehydrogenase in the L-lysine degradation pathway toward its non-cognate substrate 2-oxopimelic acid. *Int. J. Mol. Sci.* **23**, 8213 (2022).
- Leandro, J. et al. Inhibition and crystal structure of the human DHTKD1-thiamin diphosphate complex. *ACS Chem. Biol.* **15**, 2041–2047 (2020).
- Bezerra, G. A. et al. Crystal structure and interaction studies of human DHTKD1 provide insight into a mitochondrial megacomplex in lysine catabolism. *IUCr* **7**, 693–706 (2020).
- Rajashankar, K. R. et al. Crystal structure and functional analysis of lipamide dehydrogenase from *Mycobacterium tuberculosis*. *J. Biol. Chem.* **280**, 33977–33983 (2005).
- Byron, O. & Lindsay, J. G. The pyruvate dehydrogenase complex and related assemblies in health and disease. In *Macromolecular Protein Complexes* **83**, 523–550 (Macromolecular Protein Complexes, 2017).
- DeRosier, D. J., Oliver, R. M. & Reed, L. J. Crystallization and preliminary structural analysis of dihydrolipoyl transsuccinylase, the core of the 2-oxoglutarate dehydrogenase complex. *Proc. Natl Acad. Sci. USA* **68**, 1135–1137 (1971).
- Reed, L. J., Fernandez-Moran, H., Koike, M. & Wilms, C. R. Electron Microscopic And Biochemical Studies Of Pyruvate Dehydrogenase Complex Of *Escherichia coli*. *Science* **145**, 930–932 (1964).
- Mattevi, A. et al. Atomic structure of the cubic core of the pyruvate dehydrogenase multienzyme complex. *Science* **255**, 1544–1550 (1992).
- Knapp, J. E. et al. Crystal structure of the truncated cubic core component of the *Escherichia coli* 2-oxoglutarate dehydrogenase multienzyme complex. *J. Mol. Biol.* **280**, 655–68 (1998).
- Izard, T. et al. Principles of quasi-equivalence and Euclidean geometry govern the assembly of cubic and dodecahedral cores of pyruvate dehydrogenase complexes. *Proc. Natl Acad. Sci. USA* **96**, 1240–1245 (1999).
- Kato, M. et al. A synchronized substrate-gating mechanism revealed by cubic-core structure of the bovine branched-chain alpha-ketoacid dehydrogenase complex. *Embo J.* **25**, 5983–5994 (2006).
- Milne, J. L. S. et al. Molecular structure of a 9-MDa icosahedral pyruvate dehydrogenase subcomplex containing the E2 and E3 enzymes using cryoelectron microscopy. *J. Biol. Chem.* **281**, 4364–4370 (2006).
- Vijaykrishnan, S. et al. Solution structure and characterisation of the human pyruvate dehydrogenase complex core assembly. *J. Mol. Biol.* **399**, 71–93 (2010).
- Frank, R. A. W., Titman, C. M., Pratap, J. V., Luisi, B. F. & Perham, R. N. A molecular switch and proton wire synchronize the active sites in thiamine enzymes. *Science* **306**, 872–876 (2004).
- Pei, X. Y., Titman, C. M., Frank, R. A. W., Leeper, F. J. & Luisi, B. F. Snapshots of catalysis in the E1 subunit of the pyruvate dehydrogenase multienzyme complex. *Structure* **16**, 1860–1872 (2008).
- Arjunan, P. et al. Novel binding motif and new flexibility revealed by structural analyses of a pyruvate dehydrogenase-dihydrolipoyl acetyltransferase subcomplex from the *Escherichia coli* pyruvate dehydrogenase multienzyme complex. *J. Biol. Chem.* **289**, 30161–30176 (2014).
- Mande, S. S., Sarfaty, S., Allen, M. D., Perham, R. N. & Hol, W. G. Protein–protein interactions in the pyruvate dehydrogenase multienzyme complex: dihydrolipoamide dehydrogenase complexed with the binding domain of dihydrolipoamide acetyltransferase. *Structure* **4**, 277–286 (1996).
- Brautigam, C. A. et al. Structural and thermodynamic basis for weak interactions between dihydrolipoamide dehydrogenase and subunit-binding domain of the branched-chain alpha-ketoacid dehydrogenase complex. *J. Biol. Chem.* **286**, 23476–23488 (2011).
- Brautigam, C. A. et al. Structural insight into interactions between dihydrolipoamide dehydrogenase (E3) and E3 binding protein of human pyruvate dehydrogenase complex. *Structure* **14**, 611–621 (2006).
- Škerlová, J., Berndtsson, J., Nolte, H., Ott, M. & Stenmark, P. Structure of the native pyruvate dehydrogenase complex reveals the mechanism of substrate insertion. *Nat. Commun.* **12**, 5277 (2021).
- Kyrilidis, F. L. et al. Integrative structure of a 10-megadalton eukaryotic pyruvate dehydrogenase complex from native cell extracts. *Cell Rep.* **34**, 108727 (2021).
- Forsberg, B. O., Aibara, S., Howard, R. J., Mortezaei, N. & Lindahl, E. Arrangement and symmetry of the fungal E3BP-containing core of the pyruvate dehydrogenase complex. *Nat. Commun.* **11**, 4667 (2020).
- Tüting, C. et al. Cryo-EM snapshots of a native lysate provide structural insights into a metabolon-embedded transacetylase reaction. *Nat. Commun.* **12**, 6933 (2021).
- Usuda, Y. et al. Molecular cloning of the *Corynebacterium glutamicum* (“*Brevibacterium lactofermentum*” AJ12036) *odhA* gene encoding a novel type of 2-oxoglutarate dehydrogenase. *Microbiology* **142**, 3347–3354 (1996).
- Hoffelder, M., Raasch, K., Ooyen, J. van & Eggeling, L. The E2 domain of *OdhA* of *Corynebacterium glutamicum* has succinyltransferase activity dependent on lipoyl residues of the acetyltransferase AceF. *J. Bacteriol.* **192**, 5203–5211 (2010).
- Niebisch, A., Kabus, A., Schultz, C., Weil, B. & Bott, M. *Corynebacterium* protein kinase G controls 2-oxoglutarate dehydrogenase activity via the phosphorylation status of the OdhI protein. *J. Biol. Chem.* **281**, 12300–12307 (2006).
- Wagner, T., Bellinzoni, M., Wehenkel, A., O’Hare, H. M. & Alzari, P. M. Functional plasticity and allosteric regulation of α -ketoglutarate decarboxylase in central mycobacterial metabolism. *Chem. Biol.* **18**, 1011–1020 (2011).
- Tian, J. et al. *Mycobacterium tuberculosis* appears to lack alpha-ketoglutarate dehydrogenase and encodes pyruvate dehydrogenase in widely separated genes. *Mol. Microbiol.* **57**, 859–868 (2005).
- Bruch, E. M. et al. Actinobacteria challenge the paradigm: a unique protein architecture for a well-known, central metabolic complex. *Proc. Natl Acad. Sci.* **118**, e2112107118 (2021).
- Mattevi, A., Obmolova, G., Kalk, K. H., Teplyakov, A. & Hol, W. G. J. Crystallographic analysis of substrate binding and catalysis in dihydrolipoyl transacetylase (E2p). *Biochemistry* **32**, 3887–3901 (1993).

32. Wagner, T. et al. Structural insights into the functional versatility of an FHA domain protein in mycobacterial signaling. *Sci. Signal.* **12**, eaav9504 (2019).
33. Zhou, J. et al. A multipronged approach unravels unprecedented protein-protein interactions in the human 2-oxoglutarate dehydrogenase multienzyme complex. *J. Biol. Chem.* **293**, 19213–19227 (2018).
34. Hevler, J. F. et al. MRPS36 provides a structural link in the eukaryotic 2-oxoglutarate dehydrogenase complex. *Open Biol.* **13**, 220363 (2023).
35. Kinugawa, H. et al. In vitro reconstitution and characterization of pyruvate dehydrogenase and 2-oxoglutarate dehydrogenase hybrid complex from *Corynebacterium glutamicum*. *Microbiologyopen* **5**, 593–14 (2020).
36. Wagner, T., Barilone, N., Alzari, P. M. & Bellinzoni, M. A dual conformation of the post-decarboxylation intermediate is associated with distinct enzyme states in mycobacterial KGD (α -ketoglutarate decarboxylase). *Biochem J.* **457**, 425–434 (2014).
37. Wagner, T., Boyko, A., Alzari, P. M., Bunik, V. I. & Bellinzoni, M. Conformational transitions in the active site of mycobacterial 2-oxoglutarate dehydrogenase upon binding phosphonate analogues of 2-oxoglutarate: from a Michaelis-like complex to ThDP adducts. *J. Struct. Biol.* **208**, 182–190 (2019).
38. Chen, J., Noble, A. J., Kang, J. Y. & Darst, S. A. Eliminating effects of particle adsorption to the air/water interface in single-particle cryo-electron microscopy: Bacterial RNA polymerase and CHAPSO. *J. Struct. Biol. X* **1**, 100005 (2019).
39. Balakrishnan, A., Jordan, F. & Nathan, C. F. Influence of allosteric regulators on individual steps in the reaction catalyzed by *Mycobacterium tuberculosis* 2-hydroxy-3-oxoadipate synthase. *J. Biol. Chem.* **288**, 21688–21702 (2013).
40. O'Hare, H. M. et al. Regulation of glutamate metabolism by protein kinases in mycobacteria. *Mol. Microbiol.* **70**, 1408–1423 (2008).
41. Krawczyk, S. et al. The FHA domain of Odh1 interacts with the carboxyterminal 2-oxoglutarate dehydrogenase domain of OdhA in *Corynebacterium glutamicum*. *FEBS Lett.* **584**, 1463–1468 (2010).
42. Sundermeyer, L. et al. Characteristics of the GlnH and GlnX signal transduction proteins controlling PknG-mediated phosphorylation of Odh1 and 2-oxoglutarate dehydrogenase activity in *Corynebacterium glutamicum*. *Microbiol Spectr.* **10**, e02677–22 (2022).
43. Punjani, A. & Fleet, D. J. 3D variability analysis: resolving continuous flexibility and discrete heterogeneity from single particle cryo-EM. *J. Struct. Biol.* **213**, 107702 (2021).
44. Jiang, J. et al. Atomic structure of the E2 inner core of human pyruvate dehydrogenase complex. *Biochemistry* **57**, 2325–2334 (2018).
45. Liu, S., Xia, X., Zhen, J., Li, Z. & Zhou, Z. H. Structures and comparison of endogenous 2-oxoglutarate and pyruvate dehydrogenase complexes from bovine kidney. *Cell Discov.* **8**, 126 (2022).
46. Nagy, B. et al. Structure of the dihydrolipoamide succinyltransferase (E2) component of the human α -ketoglutarate dehydrogenase complex (hKGDHC) revealed by cryo-EM and cross-linking mass spectrometry: implications for the overall hKGDHC structure. *Biochim. Et. Biophys. Acta BBA Gen. Subj.* **1865**, 129889 (2021).
47. Ozohanics, O., Zhang, X., Nemeria, N. S., Ambrus, A. & Jordan, F. Probing the E1 α -E2 α and E1 β -E2 α interactions in binary sub-complexes of the human 2-oxoglutarate dehydrogenase and 2-oxoadipate dehydrogenase complexes by chemical cross-linking mass spectrometry and molecular dynamics simulation. *Int. J. Mol. Sci.* **24**, 4555 (2023).
48. Mattevi, A. How evolution dismantles and reassembles multi-enzyme complexes. *Proc. Natl Acad. Sci.* **119**, e2120286118 (2022).
49. Unger, T., Jacobovitch, Y., Dantes, A., Bernheim, R. & Peleg, Y. Applications of the Restriction Free (RF) cloning procedure for molecular manipulations and protein expression. *J. Struct. Biol.* **172**, 34–44 (2010).
50. Correa, A. et al. Generation of a vector suite for protein solubility screening. *Front. Microbiol.* **5**, 67 (2014).
51. Studier, F. W. Protein production by auto-induction in high density shaking cultures. *Protein Expr. Purif.* **41**, 207–234 (2005).
52. Berg, S., van den, Lofdahl, P. A., Hard, T. & Berglund, H. Improved solubility of TEV protease by directed evolution. *J. Biotechnol.* **121**, 291–298 (2006).
53. Weber, P. et al. High-throughput crystallization pipeline at the crystallography core facility of the institut pasteur. *Molecules* **24**, 4451 (2019).
54. Vonrhein, C. et al. Data processing and analysis with the autoPROC toolbox. *Acta Crystallogr. D. Biol. Crystallogr.* **67**, 293–302 (2011).
55. McCoy, A. J. et al. Phaser crystallographic software. *J. Appl Crystallogr* **40**, 658–674 (2007).
56. Emsley, P., Lohkamp, B., Scott, W. G. & Cowtan, K. Features and development of Coot. *Acta Crystallogr. D. Biol. Crystallogr.* **66**, 486–501 (2010).
57. Smart, O. S. et al. Exploiting structure similarity in refinement: automated NCS and target-structure restraints in BUSTER. *Acta Crystallogr. D. Biol. Crystallogr.* **68**, 368–380 (2012).
58. Williams, C. J. et al. MolProbity: More and better reference data for improved all-atom structure validation. *Protein Sci.* **27**, 293–315 (2018).
59. Liebschner, D. et al. Macromolecular structure determination using X-rays, neutrons and electrons: recent developments in Phenix. *Acta Crystallogr. D. Struct. Biol.* **75**, 861–877 (2019).
60. Morin, A. et al. Collaboration gets the most out of software. *eLife* **2**, e01456 (2013).
61. Kandiah, E. et al. CM01: a facility for cryo-electron microscopy at the European Synchrotron. *Acta Crystallogr. Sect. D. Struct. Biol.* **75**, 528–535 (2019).
62. Punjani, A., Rubinstein, J. L., Fleet, D. J. & Brubaker, M. A. cryoSPARC: algorithms for rapid unsupervised cryo-EM structure determination. *Nat. Methods* **14**, 290–296 (2017).
63. Pettersen, E. F. et al. UCSF Chimera—a visualization system for exploratory research and analysis. *J. Comput. Chem.* **25**, 1605–1612 (2004).
64. Raasch, K. et al. Interaction of 2-oxoglutarate dehydrogenase OdhA with its inhibitor Odh1 in *Corynebacterium glutamicum*: Mutants and a model. *J. Biotechnol.* **191**, 99–105 (2014).
65. Yamashita, K., Palmer, C. M., Burnley, T. & Murshudov, G. N. Cryo-EM single-particle structure refinement and map calculation using Servalcat. *Acta Crystallogr. Sect. D. Struct. Biol.* **77**, 1282–1291 (2021).
66. Burnley, T., Palmer, C. M. & Winn, M. Recent developments in the CCP-EM software suite. *Acta Crystallogr. Sect. D. Struct. Biol.* **73**, 469–477 (2017).
67. Pettersen, E. F. et al. UCSF ChimeraX: structure visualization for researchers, educators, and developers. *Protein Sci.* **30**, 70–82 (2021).
68. Schrödinger, LLC. *The PyMOL Molecular Graphics System*, v. 2.5.4. <https://pymol.org/2/> (2022).
69. Schuck, P. Size-distribution analysis of macromolecules by sedimentation velocity ultracentrifugation and lamm equation modeling. *Biophys. J.* **78**, 1606–1619 (2000).
70. Johnson, L. S., Eddy, S. R. & Portugaly, E. Hidden Markov model speed heuristic and iterative HMM search procedure. *BMC Bioinform.* **11**, 431 (2010).
71. Sayers, E. W. et al. GenBank. *Nucleic Acids Res.* **49**, gkaa1023 (2020).

72. Katoh, K. & Standley, D. M. MAFFT multiple sequence alignment software version 7: improvements in performance and usability. *Mol. Biol. Evol.* **30**, 772–780 (2013).
73. Crooks, G. E., Hon, G., Chandonia, J.-M. & Brenner, S. E. WebLogo: a sequence logo generator. *Genome Res.* **14**, 1188–1190 (2004).
74. Robert, X. & Gouet, P. Deciphering key features in protein structures with the new ENDScript server. *Nucleic Acids Res.* **42**, W320–W324 (2014).

Acknowledgements

This work was funded by the ANR projects SUPERCLX (ANR-13-JSV8-0003) and METACTINO (ANR-18-CE92-0003), both granted to M.B., and by institutional funds from the Institut Pasteur, the CNRS and the Université Paris Cité. We are grateful to the core facilities at the Institut Pasteur C2RT (Center for Technological Resources and Research) and their respective staff, namely to A. Haouz, P. Weber and C. Pissis for performing crystallization screenings, B. Raynal, S. Brûlé and S. Hoos for their assistance in analytical ultracentrifugation and buffer optimization, P. England for his help with surface plasmon resonance experiments, J.-M. Winter, S. Tachon and M. Vos for assistance with EM data collection. We are also grateful to N. Barilone, I. Miras and P. Vilela for their initial work in construct generation and protein expression, to A. Bezault, G. Péhau-Arnaudet and C. Rapisarda for their help in grid preparation and EM data collection, and to M. Bott and B.J. Eikmanns for insightful discussions. We acknowledge the synchrotron sources Soleil (Saint-Aubin, France), and ESRF (Grenoble, France) for granting access to their facilities, and their respective staff for helpful assistance, in particular E. Kandiah for performing EM data collection on CM01 (ESRF). The Nanomaging Core at Institut Pasteur was created with the help of a grant from the French Government's 'Investissements d'Avenir' program (EQUIPEX CACSICE, ANR-11-EQPX-0008), and is acknowledged for support with cryo-EM sample preparation, image acquisition and analysis. L.Y. and A.B. have both been affiliated to the Pasteur – Paris University (PPU) International PhD program; L.Y. was funded by the Wuhan Institute of Biological Products Co. Ltd. (Wuhan, People's Republic of China), subsidiary company of China National Biotec Group Company Limited, and by a doctoral fellowship from the China Scholarship Council (CSC). Succinyl phosphonate was a kind gift from V. Bunik (Lomonosov University, Moscow); TEV expression plasmid was provided by H. Berglund (Karolinska Institute, Stockholm).

Author contributions

L.Y., T.W., A.B. and E.M.B. produced and purified recombinant proteins; L.Y., T.W., A.B., F.G. and M.B. collected data; L.Y. prepared cryo-EM

grids; L.Y. and A.M. analyzed cryo-EM data; L.Y., T.W., A.M. and M.B. refined models; L.Y. performed biophysical experiments; A.B. performed enzymatic activity assays; D.M. performed bioinformatic analysis; P.M.A. provided advice on data interpretation and contributed to the manuscript; M.B. supervised the work and wrote the paper. All authors reviewed the manuscript and agreed on its content.

Competing interests

The authors declare no competing interests.

Additional information

Supplementary information The online version contains supplementary material available at <https://doi.org/10.1038/s41467-023-40253-6>.

Correspondence and requests for materials should be addressed to Marco Bellinzoni.

Peer review information *Nature Communications* thanks the anonymous reviewers for their contribution to the peer review of this work. A peer review file is available.

Reprints and permissions information is available at <http://www.nature.com/reprints>

Publisher's note Springer Nature remains neutral with regard to jurisdictional claims in published maps and institutional affiliations.

Open Access This article is licensed under a Creative Commons Attribution 4.0 International License, which permits use, sharing, adaptation, distribution and reproduction in any medium or format, as long as you give appropriate credit to the original author(s) and the source, provide a link to the Creative Commons license, and indicate if changes were made. The images or other third party material in this article are included in the article's Creative Commons license, unless indicated otherwise in a credit line to the material. If material is not included in the article's Creative Commons license and your intended use is not permitted by statutory regulation or exceeds the permitted use, you will need to obtain permission directly from the copyright holder. To view a copy of this license, visit <http://creativecommons.org/licenses/by/4.0/>.

© The Author(s) 2023